frontiers | Frontiers in Physics

TYPE Original Research
PUBLISHED 02 December 2025
DOI 10.3389/fphy.2025.1689932

OPEN ACCESS

EDITED BY
Venugopal Rao Soma,
University of Hyderabad, India

REVIEWED BY
Xiao Sun,
Curtin University, Australia
Songyan Hou,
Xidian University, China

*CORRESPONDENCE
Youyou Hu,
yyhu@just.edu.cn
Dahuai Zheng,
dhzheng@nankai.edu.cn
Yongfa Kong,
kongyf@nankai.edu.cn

RECEIVED 21 August 2025
REVISED 18 November 2025
ACCEPTED 19 November 2025
PUBLISHED 02 December 2025

CITATION
Wang S, Wang W, Zhang Y, Hu Y, Zheng D, Liu H and Kong Y (2025) Improvement of the photorefractive response in bismuth and magnesium co-doped lithium niobate crystals via oxygen-vacancy modulation through controlled redox annealing.
Front. Phys. 13:1689932.
doi: 10.3389/fphy.2025.1689932

Improvement of the photorefractive response in bismuth and magnesium co-doped lithium niobate crystals via oxygen-vacancy modulation through controlled redox annealing

Shuolin Wang[1], Weiwei Wang[2], Yuqi Zhang[3], Youyou Hu[1]*, Dahuai Zheng[3]*, Hongde Liu[3] and Yongfa Kong[3]*

[1]College of Science, Jiangsu University of Science and Technology, Zhenjiang, China, [2]Department of Mathematics and Physics, Shijiazhuang Tiedao University, Shijiazhuang, China, [3]MOE Key Laboratory of Weak-Light Nonlinear Photonics, TEDA Institute of Applied Physics and School of Physics, Nankai University, Tianjin, China

In this study, bismuth (Bi) and magnesium (Mg) co-doped lithium niobate crystals (LN:Bi,$Mg_{6.0}$) with a rapid photorefractive (PR) response were subjected to annealing treatments in oxygen and various argon atmospheres to modulate their oxidation-reduction states. The PR properties of LN:Bi,$Mg_{6.0}$ crystals with different redox states, including saturation diffraction efficiency, response time, and sensitivity, were systematically characterized at laser wavelengths of 532 nm, 488 nm, and 442 nm. The results demonstrate that reduction treatment effectively shortens the response time and enhances the PR sensitivity of LN:Bi,$Mg_{6.0}$ crystals. In particular, the crystal reduced in Ar atmosphere for 24 h exhibited a response time of 5.4 m at 442 nm, representing a 58% reduction compared to the as-grown crystal. O *1s* X-ray photoelectron spectroscopy (XPS) revealed that changes in the redox state directly affect the concentration of oxygen vacancies (V_O) in the crystal, thereby influencing its PR performance. As the V_O increases, the PR response time initially decreases and then increases. In addition, based on the results of ultraviolet-visible (UV-Vis) absorption spectra and XPS, the defect structures of LN:Bi,$Mg_{6.0}$ crystal with varying redox states were discussed.

KEYWORDS

$LiNbO_3$ crystal, photorefraction, rapid response, redox annealing, oxygen-vacancy

Introduction

In recent years, the commercialization of advanced three-dimensional (3D) display technologies, including holographic glasses and automotive augmented reality head-up displays (AR-HUDs), has ushered in a new era of immersive interaction by seamlessly merging virtual and real-world elements. Among these innovations, holographic 3D

display stands out as the most promising next-generation visual technology, primarily due to its inherent advantage of enabling naked-eye viewing without the need for additional eyewear [1–5]. Optical holographic display based on photorefractive (PR) materials is one of the most effective approaches to achieving real-time dynamic 3D visualization [6]. The PR effect involves two fundamental physical processes: first, the photoconductive process, in which photoexcited charge carriers are generated and redistributed to form a spatial space-charge field; and second, the electro-optic process, where this field induces a refractive index modulation through the Pockels effect [7]. This light-induced refractive index change provides a direct mechanism for dynamic holographic recording. Owing to its reversibility and real-time tunability, the PR effect enables continuous writing and erasing of holographic gratings, thereby making PR materials highly promising for real-time dynamic holographic 3D displays [8]. Although organic polymers [9] and liquid crystals [10, 11] are widely adopted in current display systems, they encounter critical challenges including material degradation and the requirement for high operational voltages. In contrast, inorganic PR crystals have emerged as ideal candidates for dynamic holographic displays due to their stable physicochemical properties and the ability to achieve high diffraction efficiency without the need for external voltage.

Lithium niobate ($LiNbO_3$, LN) crystal, called "silicon of photonics", is one of multi-functional artificial crystal that combines excellent physical properties such as electro-optic, acousto-optic, piezoelectric, nonlinear optical properties, and PR effects [12–18]. Based on these attractive properties, LN has played a prominent role in many recent technological achievements, such as modulators [19–22], permanent holographic recording equipment [23], nonlinear resonators [24, 25], and integrated optics on-chip [26–28]. However, as a classic inorganic PR material, the slow response time of LN crystals has long limited their use in holographic displays [29–31]. Recent studies have revealed that co-doping LN crystals with Mg^{2+} and lone-pair electron cations (e.g., Bi^{3+}, Sb^{3+}) significantly enhances the PR response speed [32–34]. Specifically, for a Bi and Mg co-doped LN crystal (LN:$Bi_{1.0}$,$Mg_{6.0}$), the response time was reduced to 13 m at 442 nm [35]. Although increasing the Bi^{3+} doping concentration further shortened the response time to 7.2 m in LN:$Bi_{2.0}$,$Mg_{6.0}$ crystals, enabling real-time dynamic holographic display at a 60 Hz refresh rate [36], this improvement came at the expense of significantly degraded crystal quality. Therefore, it is crucial to investigate whether the response time can be shortened while maintaining crystal quality to achieve high refresh rates.

In this work, a 1.0 mol% Bi and 6.0 mol% Mg co-doped LN crystal (LN:Bi,$Mg_{6.0}$) was grown via the Czochralski (CZ) method, and subsequently, the redox states of LN:Bi,$Mg_{6.0}$ samples were modulated through annealing under O_2 and Ar atmospheres, respectively. The PR properties of as-grown and redox-treated samples were systematically evaluated. Ultraviolet-visible (UV-Vis) spectroscopy and X-ray photoelectron spectroscopy (XPS) analyses were performed to investigate defect structures. The results demonstrate that optimizing the concentration ratio between oxygen vacancies (V_O) and lattice oxygen can reduce the PR response time of LN:Bi,$Mg_{6.0}$ crystals by 58% at 442 nm.

Materials and methods

Sample preparation

A congruent LN (CLN) crystal with a composition of [Li]/[Nb] = 48.6/51.4, co-doped with 1.0 mol% of Bi and 6.0 mol% Mg, was grown along the z-axis using the CZ method and labeled as LN:Bi,$Mg_{6.0}$. The specific steps and detailed parameters involved in crystal growth are provided in the Supplementary Material. The crystal was maintained at 1,210 °C for 24 h for annealing, followed by 1-h polarization with a 50 mA current at the same temperature, and then controllably cooled to room temperature to complete the annealing and polarization process, thereby eliminating internal thermal stresses and ensuring single-domain formation. Subsequently, five y-oriented wafers with identical dimensions of 10*8*1 mm (length*width*thicknesses) were prepared for redox treatment. Among the five samples, one was left untreated, while the other four underwent distinct thermal treatments under controlled atmospheres:

1. Three samples were individually subjected to reduction treatments in an argon atmosphere (flow rate: 1.4 L/min). The temperature was raised to 500 °C in 5 h, held isothermally for either 12 h, 24 h, or 36 h, and then cooled to room temperature in 5 h.
2. The remaining sample was treated in an oxygen atmosphere (flow rate: 1.4 L/min), during which the temperature was increased to 800 °C in 5 h, held for 12 h, and then cooled to room temperature in 5 h.

The samples are labeled according to their treatment conditions: the untreated sample is labeled "As-grown"; three argon-reduced samples with 12, 24, and 36 h isothermal holds are labeled "Ar-12 h", "Ar-24 h", and "Ar-36 h", respectively; and the oxygen-oxidized sample with 12 h isothermal hold is labeled "O_2-12 h".

Experimental methods

The two-wave coupling method [32] was employed to characterize the PR properties of LN:Bi,Mg crystals subjected to different treatment conditions. According to the coupled-wave theory, two coherent beams with identical frequency and polarization interfere inside the crystal and generate a spatially modulated space-charge field. Based on the PR theory, this space-charge field induces a refractive-index modulation that follows the interference pattern, thereby forming a volume phase grating within the crystal. Under these conditions, a cosine-type intensity modulation is established in the crystal, and the light-intensity coupling can be described by Equation 1:

$$\begin{cases} cos\,\theta \dfrac{dI_1}{dx} = -\Gamma \dfrac{I_1 I_2}{I_1 + I_2} - \alpha I_1 \\ cos\,\theta \dfrac{dI_2}{dx} = \Gamma \dfrac{I_1 I_2}{I_1 + I_2} - \alpha I_2 \end{cases} \tag{1}$$

Here, $\Gamma = \frac{2\pi n_1}{\lambda cos\,\theta} sin\,\phi$ is the intensity–coupling coefficient. The refractive-index modulation is given by $n_1 = -n_0^3 \gamma E_{sc}$, where E_{sc} is the space–charge field and ϕ denotes the spatial phase shift between the induced index grating and the optical interference pattern.

Experimental results show that the PR process in LN:Bi,Mg crystals is dominated by the diffusion mechanism, and electrons act as the primary charge carriers [35]. Under these conditions, the phase shift is $\phi = -\pi/2$, and α represents the absorption coefficient. For the boundary conditions $I_1(x=0) = I_{10}$ and $I_2(x=0) = I_{20}$, with $I_{10} = I_{20}$ and $I_{10} + I_{20} = I_0$, the solution of Equation 1 is shown as Equation 2:

$$\begin{cases} I_1 = \dfrac{I_0}{1+e^{\Gamma x/\cos\theta}} e^{-\alpha x/\cos\theta} \\ I_2 = \dfrac{I_0}{1+e^{\Gamma x/\cos\theta}} e^{(\Gamma-\alpha)x/\cos\theta} \end{cases} \tag{2}$$

Three laser wavelengths were selected for the measurements: 532 nm from a continuous-wave frequency-doubled solid-state laser, 488 nm from an Ar^+ laser, and 442 nm from a He-Cd laser. Figure 1 presented the schematic drawing of the experimental set-up used for PR properties measurement. The laser beam was split into two beams of equal intensity I_s and I_R (400 mW/cm^2 for each beam) by splitter mirror and the sample was irradiated at an angle of 30° (@532 nm), 27° (@488 nm), and 24.5° (@442 nm), respectively. The vector of the grating was parallel to the *c*-axis for obtaining the maximum electro-optical constant γ_{33}. The 633 nm beam emitted from the He-Ne laser was used as the monitoring light, which is incident from a strict Bragg angle. A weak 633 nm He-Ne probe beam (3 mW/cm^2) incident at the exact Bragg angle monitored grating formation without affecting photorefraction. PD3 and PD4 were used to record the diffraction efficiency data in real time by controlling the shutter switch. The diffraction efficiency (η) of the crystals is defined as Equation 3:

$$\eta = I_d/(I_d + I_t) \tag{3}$$

where "I_d" is the diffracted beam intensity, "I_t" is the transmitted beam intensity. The temporal evolution of diffraction efficiency (η) can be expressed as Equation 4:

$$\eta_t = \eta_s\left(1 - e^{-t/\tau_r}\right)^2 \tag{4}$$

where η_t is the diffraction efficiency at time t, η_s is the saturated diffraction efficiency, and τ_r is the response time of the crystal, which are determined by fitting the experimental curve of η versus t. Further, the sensitivity (S) of the crystal is defined as Equation 5:

$$S = \left(\left(\partial\sqrt{\eta}\right)/\partial t\right)_{t=0}/Id \tag{5}$$

where "d" is the thickness of the crystal, "I" represents the light intensity.

Computational details

All the calculations in this work are done using the Vienna Ab initio Simulation Package (VASP) [37, 38] which performs an iterative solution of the Kohn–Sham equations with a plane-wave basis set. The energy cutoff for plane waves was 400 eV. The projector augmented wave (PAW) method was used to describe the electron-ion interactions. The Perdew-Burke-Ernzerh (PBE) function was adopted to treat the electron exchange and correlation energy [39, 40]. A 2 × 2 × 2 supercell of 240 atoms is used in the calculations. The K-mesh is chosen as 2 × 2 × 2, which is fine enough to give a reasonable result. For all the calculations, the structure is optimized with a force convergence criterion of 0.01 eV/Å.

Results and discussions

Figure 2a presents the saturated diffraction efficiency (η_s) of "As-grown", "Ar-12 h", "Ar-24 h", "Ar-36 h", and "O_2-12 h" LN:Bi,$Mg_{6.0}$ samples. Compared to the η_s of "As-grown" and "O_2-12 h" samples, the η_s of the three samples subjected to Ar-reduction treatments decreased at all three laser wavelengths of 532, 488, and 442 nm. The response time (τ_r) of these five samples is shown in Figure 2b. For clarity, the τ_r is displayed on a logarithmic scale owing to its large variation over several orders of magnitude at the three measured wavelengths. After Ar-reduction treatments, the τ_r of "Ar-12 h", "Ar-24 h", and "Ar-36 h" samples was significantly shortened at all three wavelengths. As the duration of the reduction treatment increased, the response time initially decreased and then slightly increased. Notably, the τ_r of "Ar-24 h" sample reached a minimum of 250 m, 92 m, and 5.4 m at 532 nm, 488 nm, and 442 nm, respectively. Similarly, in Figure 2c, a logarithmic y-axis is also employed to display the sensitivities (*S*) of all five samples measured at 532 nm, 488 nm, and 442 nm. It's not difficult to find that Ar-reduction treatment effectively enhances the *S* of LN:Bi,$Mg_{6.0}$ crystal. Especially, the *S* of "Ar-24 h" sample reached maximum values of 7.79 cm/J, 35.89 cm/J, and 713.89 cm/J at 532 nm, 488 nm, and 442 nm, respectively.

The above results demonstrate that Ar-reduction treatments can effectively reduce the response time and enhance the PR sensitivity of LN:Bi,$Mg_{6.0}$. Notably, for "Ar-24 h" sample, the response time was significantly shortened by 71%, 46%, and 58% at the three measured wavelengths compared to that of "As-grown" sample. Specifically, at 442 nm, the response time of "Ar-24 h" sample decreased by nearly 2 m, while the PR sensitivity increased by 10% relative to the LN:$Bi_{2.0}$,$Mg_{6.0}$ crystal [36].

The UV-Visible absorption spectra of LN crystals exhibit high sensitivity to their composition and defect energy levels [41, 42]. The fundamental optical absorption edge is primarily determined by the charge transfer transition energy from oxygen (O) 2*p* orbitals to niobium (Nb) 4*d* orbitals. Redox treatments can significantly influence the electron cloud distribution around O atoms in the lattice, thereby modifying the bonding strength of Nb-O bonds. These changes directly affect the bandgap. By monitoring shifts in the absorption edge and spectral variations in UV-Vis spectra, the impact of redox treatments on the defect structure of LN:Bi,$Mg_{6.0}$ crystal can be investigated. Figure 3a presents the UV-Vis absorption spectra (300–800 nm) of "As-grown", "Ar-12 h", "Ar-24 h", "Ar-36 h", and "O_2-12 h" 1-mm-thick LN:Bi,$Mg_{6.0}$ samples. The absorption edge of LN crystals is typically defined at the wavelength corresponding to an absorption coefficient of 15 or 20 cm^{-1}; in this study, 20 cm^{-1} was selected as the reference point. Notably, "O_2-12 h" sample exhibits a distinct red shift, whereas Ar atmosphere reduction results in negligible shift compared to the as-grown crystal.

According to the Li vacancy model, the dominant intrinsic defects in CLN are V_{Li}^- and Nb_{Li}^{4+}. However, in LN:Bi,Mg crystals with Mg concentrations above the threshold, the intrinsic Nb_{Li}^{4+} defects disappear, leaving V_{Li}^-, Mg_{Li}^+, Mg_{Nb}^{3-}, Bi_{Nb}^{2-}, and Bi_{Li}^{2+} as the predominant defects. Previous studies report that the absorption edge of LN crystals is intrinsically correlated with the concentration of V_{Li}^- [43]. Typically, an increase in V_{Li}^- concentration leads to bandgap narrowing, consequently resulting

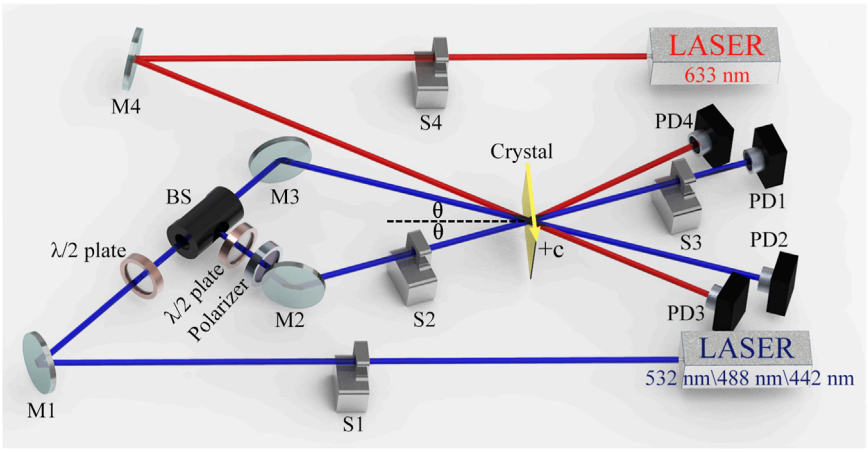

FIGURE 1
Schematic diagram of the two-wave coupling experimental setup.

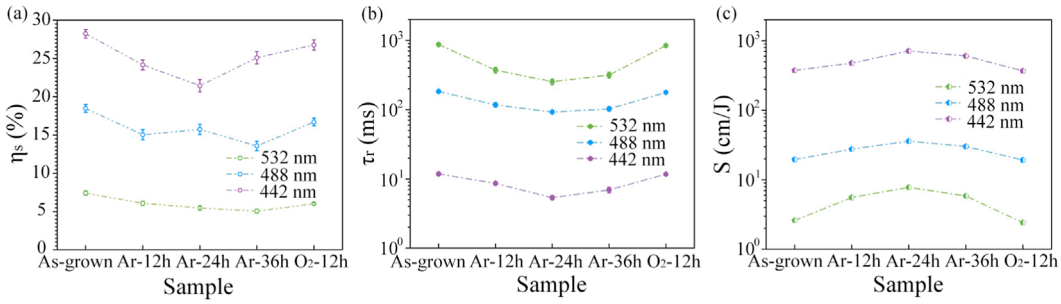

FIGURE 2
Saturated Diffraction Efficiency η_s **(a)**, Response time τ_r **(b)**, and Sensitivity S **(c)** of "As-grown", "Ar-12 h", "Ar-24 h", "Ar-36 h", and "O_2-12 h" LN:Bi,$Mg_{6.0}$ samples, measured at 532 nm, 488 nm, and 442 nm, respectively. Detailed measurement data are provided in the Supplementary Material.

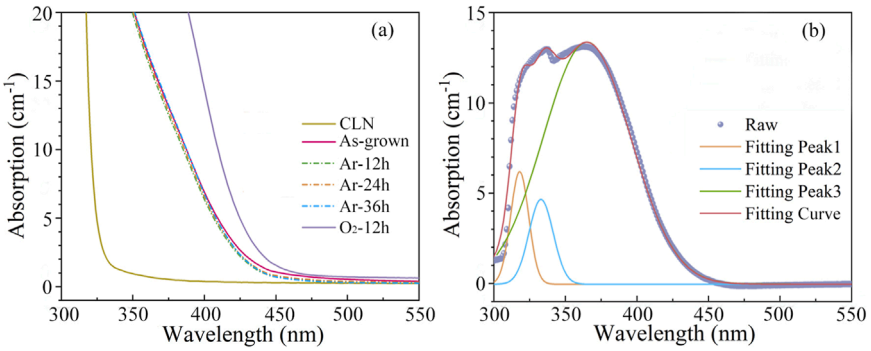

FIGURE 3
(a) UV-Vis Absorption spectra of CLN and "As-grown", "Ar-12 h", "Ar-24 h", "Ar-36 h", and "O_2-12 h" LN:Bi,$Mg_{6.0}$ samples. **(b)** Absorption difference between "O_2-12 h" and "As-grown" LN:Bi,$Mg_{6.0}$ samples.

in a red shift of the absorption edge [44]. Upon oxidation treatment, part of Bi_{Li}^{2+} and Bi_{Nb}^{2-} oxidize to form Bi_{Li}^{4+} and Bi_{Nb}^{0}. To maintain charge neutrality, this process requires additional V_{Li}^{-} for charge compensation. The increased valence state of Bi ions during oxidation necessarily leads to an elevation in V_{Li}^{-} concentration, which in turn causes the observed red shift of the absorption edge. Meanwhile, theoretical calculations of the band structure of LN containing $Bi_{Li}^{2+/4+}$ and $Bi_{Nb}^{2-/0}$ point defects indicate that both Bi_{Li}^{4+} and Bi_{Nb}^{0} can narrow the band gap of LN. For specific details regarding the band structure, please refer to the

TABLE 1 Fitting results of "O_2-12 h" LN:Bi,$Mg_{6.0}$ sample absorption difference spectrum.

Sample	Peak1	Peak2	Peak3
O_2-12 h	318.23 ± 0.78	330.35 ± 1.27	365.56 ± 1.12

Supplementary Material. To further analyze the defect states in "O_2-12 h" LN:Bi,$Mg_{6.0}$ sample, differential absorption spectrum was obtained by subtracting the absorption spectrum of "As-grown" LN:Bi,$Mg_{6.0}$ sample from that of "O_2-12 h" LN:Bi,$Mg_{6.0}$ sample, as shown in Figure 3b. Gaussian fitting analysis revealed that three-peak fitting provided more accurate and physically reasonable results compared to two- or four-peak models, and the detailed peak fitting results are shown in Table 1. The absorption peak centered near 318 nm is primarily attributed to the O^{2-}-V_{Li}^{-} defect cluster. Furthermore, theoretical calculations confirm that the energy level of Bi_{Li}^{4+} point defects lies deeper than that of Bi_{Nb}^{0}. Consequently, the absorption peaks at 330 nm and 365 nm are assigned to O^{2-}-Bi_{Li}^{4+} and O^{2-}-Bi_{Nb}^{0}, respectively.

X-ray photoelectron spectroscopy (XPS) was employed to characterize the elemental composition, chemical states, and valence states of the crystalline samples [45]. To further investigate the defects and charge-state changes induced by redox treatments, O *1s* XPS characterization was performed on the CLN, "As-grown", "Ar-12 h", "Ar-24 h", "Ar-36 h", and "O_2-12 h" samples. Figure 4 shows the O *1s* XPS spectra and their fitted components for these six samples. Since the raw XPS data already include instrument-generated baseline curves, these baselines were directly subtracted prior to peak analysis. A three-peak Gaussian fitting model was adopted, corresponding to lattice oxygen, oxygen vacancies (V_O), and surface-adsorbed H_2O/OH^- [46, 47]. The fitted results display that the O *1s* spectra of all samples are well described by three Gaussian components: O_I peak at 530.16–530.73, O_{II} peak at 531.76–532.83, and O_{III} peak at 532.48–534.43 eV. The O_I peak with lower binding energy is attributed to O^{2-} in lattice sites, while the O_{II} peak corresponds to V_O, and the higher-binding-energy O_{III} peak likely originates from surface-adsorbed H_2O/OH^- [46, 47]. Additional details of the peak-fitting procedure are provided in the Supplementary Material. The ratio of O_{II} to O_I peak areas provides a semi-quantitative measure of the relative concentrations between V_O and lattice oxygen in the crystals. Our calculations yield the following O_{II}/O_I ratios: 0.32 for CLN, 0.59 for "As-grown" LN:Bi,$Mg_{6.0}$ sample, 1.16 for "Ar-12 h" sample, 1.68 for "Ar-24 h" sample, and 4.88 for "Ar-36 h" sample, while "O_2-12 h" sample exhibits a ratio of 0.28.

Compared to CLN, the increased O_{II}/O_I ratio in "As-grown" sample indicates higher V_O concentration. This phenomenon originates from a charge compensation mechanism: when Mg^{2+} doping concentration exceeds the threshold level, both Bi^{3+} and Mg^{2+} ions occupy regular Nb^{5+} sites, thereby generating V_O to maintain local charge balance within the crystal lattice. Furthermore, redox treatments can substantially modulate the relative concentrations of lattice oxygen and V_O. Specifically, oxidation decreases the V_O concentration, whereas reduction significantly increases V_O density in the crystals.

Two-wave coupling experiments clearly demonstrate that Ar-reduction treatment effectively enhances the PR response speed in LN:Bi,$Mg_{6.0}$ crystals. As reduction duration increases, the PR response time first decreases and then increases, exhibiting a non-monotonic trend at all three measured wavelengths. This behavior indicates that V_O concentration significantly influences the PR response of LN:Bi,$Mg_{6.0}$ crystals. In LN:Bi,$Mg_{6.0}$ crystals, the PR process is dominated by the diffusion mechanism, the diffusion coefficient (D) is given by $(\mu k_B T)/e$, where μ represents electron mobility, k_B is Boltzmann's constant, T denotes temperature, and e is electron charge [36]. This establishes the direct proportionality between D and μ. During Ar-atmosphere reduction, V_O tends to combine with point defects in LN:Bi,$Mg_{6.0}$ crystals, forming new defect complexes. Since the crystal must maintain overall charge neutrality and the V_O is positively charged, it preferentially associates with negatively charged centers such as Bi_{Nb}^{2-} and Mg_{Nb}^{3-}, leading to the formation of Bi_{Nb}-V_O and Mg_{Nb}-V_O. Therefore, the Ar-reduction treatment modifies the V_O concentration in LN:Bi,$Mg_{6.0}$ crystals, which leads to the formation of new defect clusters. These complexes influence electron mobility and, consequently, affect the PR response of the crystals. In fact, binding energy calculations provide a basis for understanding this process. Binding energy E_b as a criterion for judging the stability of a defect pair X_1X_2, usually be defined in terms of the formation energies E_f (see Equation 6) [48, 49]

$$E_b[(X_1X_2)^q] = E_f[(X_1X_2)^q] - E_f[(X_1)^{q_1}] - E_f[(X_2)^{q_2}] \quad (6)$$

where $q = q_1 + q_2$, the negative binding energy means that the energy required to separate the defect pair into two individual defects X_1 and X_2 is more than the formation energy of defect pair X_1X_2, which indicates a stable defect pair. As shown in Table 2, the binding energy of Bi_{Nb}-V_O is lower than that of Mg_{Nb}-V_O, demonstrating that Bi_{Nb}-V_O is more stable. During Ar reduction, the increased V_O concentration promotes the preferential formation of Bi_{Nb}-V_O complexes. These defects enhance charge transport through rapid electron capture/emission processes, thereby improving carrier mobility, accelerating space charge field formation, and ultimately shortening the response time. However, as the concentration of V_O continues to increase, some V_O defects may combine with Mg_{Nb}^{3-} to form Mg_{Nb}-V_O. As the same time, local lattice distortions become more pronounced. These combined effects hinder efficient carrier transition, which in turn results in an extended PR response.

In addition, the O *1s* peak-fitting results revealed by XPS further support this interpretation. The O_{II}/O_I peak-area ratio exhibits a monotonic increase with extended Ar reduction, reflecting the progressive rise in the relative V_O concentration across the samples. It should be noted that this ratio does not provide the absolute V_O concentration but can indicate the trend of V_O evolution under different redox treatments. When these XPS results are considered together with the calculated binding energies of defect clusters, a consistent explanation can be obtained. Since the Bi_{Nb}-V_O has a lower binding energy than Mg_{Nb}-V_O, V_O preferentially forms complexes with Bi_{Nb}^{2-} during moderate reduction, forming stable Bi_{Nb}-V_O that enhance carrier mobility and accelerate space-charge-field buildup, leading to the fastest response in the "Ar-24 h" sample. However, for the "Ar-36 h" sample under excessive reduction, the sharply increased relative V_O content promotes additional Mg_{Nb}-V_O and stronger lattice distortion, which hinder charge transport and result in a slightly slower response.

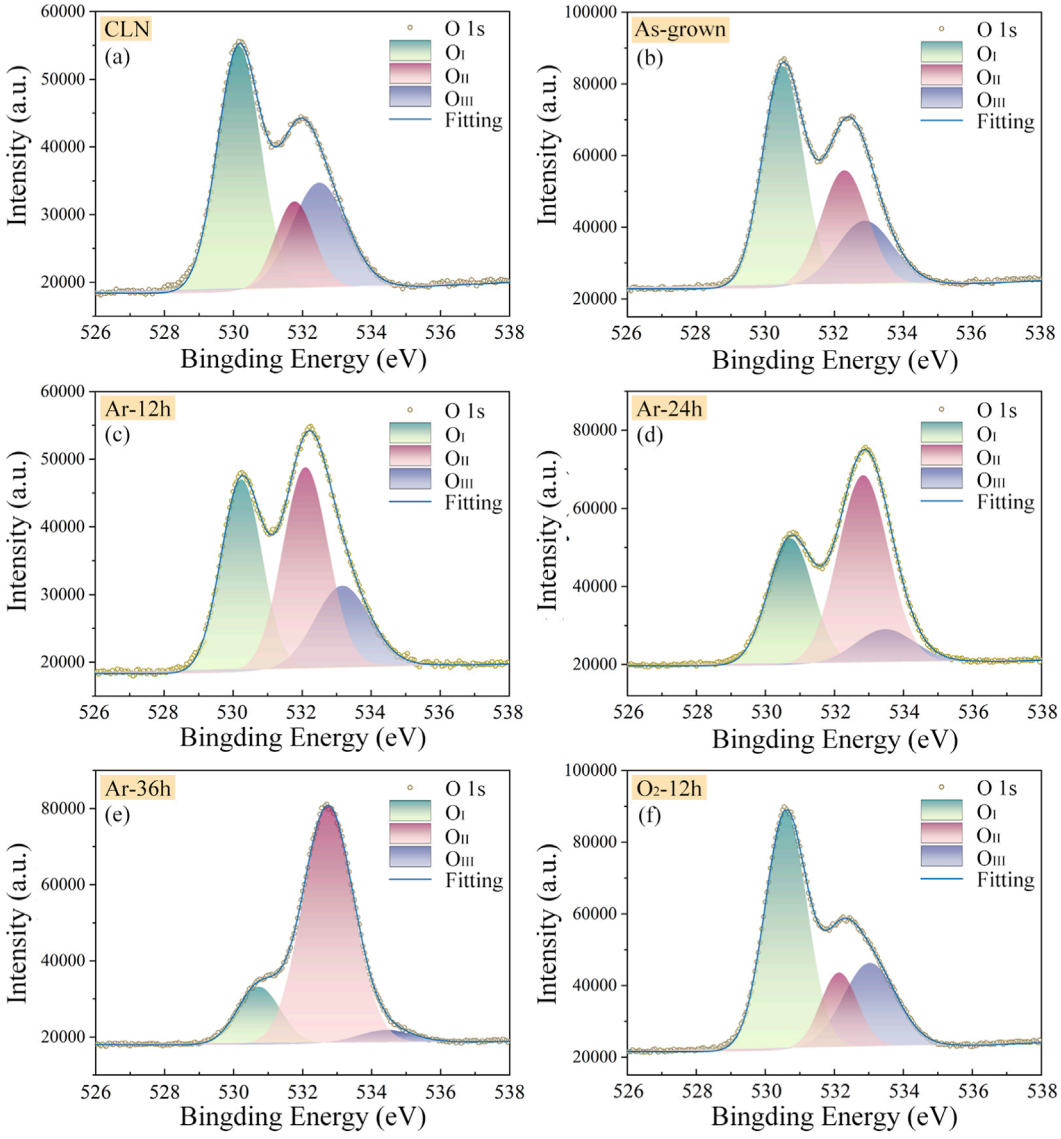

FIGURE 4
O1s XPS and peak-fitting spectra of CLN **(a)**, "As-grown" **(b)**, "Ar-12 h" **(c)**, "Ar-24 h" **(d)**, "Ar-36 h" **(e)**, and "O_2-12 h" **(f)** samples.

TABLE 2 Binding energy of the defect pairs Bi_{Nb}-V_O and Mg_{Nb}-V_O of LN:Bi,$Mg_{6.0}$ crystal.

System	E_b (eV)
Bi_{Nb}-V_O	−26.4718
Mg_{Nb}-V_O	−24.5764

Conclusion

In summary, oxidation and reduction treatments were applied to the rapid response LN:Bi,$Mg_{6.0}$ crystals. The results demonstrate that reduction treatments effectively shorten the PR response time and enhance the PR sensitivity of the crystals. In particular, the crystal reduced in Ar atmosphere for 24 h achieved a response time of 5.4 m at 442 nm, representing a 58% reduction compared to the as-grown crystal. Furthermore, XPS analysis reveals that changes in the redox state directly affect the concentration of V_O in the crystal, thereby influencing its PR performance. For 24 h Ar-reduced LN:Bi,$Mg_{6.0}$ crystal, the ratio of V_O to lattice oxygen peak areas reached 1.68, corresponding to the fastest PR response observed at all three measured wavelengths. This work provides a basis for optimizing the PR properties of Nb-site-doped LN crystals by tailoring their redox states through thermal treatment.

Data availability statement

The original contributions presented in the study are included in the article/Supplementary Material, further inquiries can be directed to the corresponding authors.

Author contributions

SW: Data curation, Formal Analysis, Writing – original draft, Writing – review and editing. WW: Methodology, Resources, Writing – review and editing. YZ: Data curation, Writing – review and editing. YH: Funding acquisition, Resources, Software, Writing – review and editing. DZ: Resources, Writing – review and editing, Methodology. HL: Conceptualization, Resources, Writing – review and editing. YK: Conceptualization, Resources, Supervision, Writing – review and editing.

Funding

The authors declare that financial support was received for the research and/or publication of this article. This work was supported by Jiangsu Provincial Key Research and Development Program (Grant No. BE2022143), Science Research Project of Hebei Education Department QN2025121, National Key Research and Development Program of China (Grant No. 2019YFA0705000), National Natural Science Foundation of China (Nos 12034010, 12134007).

Conflict of interest

The authors declare that the research was conducted in the absence of any commercial or financial relationships that could be construed as a potential conflict of interest.

Generative AI statement

The authors declare that no Generative AI was used in the creation of this manuscript.

Any alternative text (alt text) provided alongside figures in this article has been generated by Frontiers with the support of artificial intelligence and reasonable efforts have been made to ensure accuracy, including review by the authors wherever possible. If you identify any issues, please contact us.

Publisher's note

Supplementary material

The Supplementary Material for this article can be found online at: https://www.frontiersin.org/articles/10.3389/fphy.2025.1689932/full#supplementary-material

References

1. Gopakumar M, Lee GY, Choi S, Chao B, Peng Y, Kim J, et al. Full-colour 3D holographic augmented-reality displays with metasurface waveguides. *Nature* (2024) 629:791–7. doi:10.1038/s41586-024-07386-0

2. Zhang Y, Cheng D, Wang Y, Wang Y, Shan Y, Yang T, et al. Real-time multi-depth holographic display using complex-valued neural network. *Opt Express* (2025) 33(4):7380–95. doi:10.1364/oe.551943

3. Yin Y, Jiang Q, Wang H, Huang L. Color holographic display based on complex-amplitude metasurface. *Laser and Photon Rev* (2025) 19(1):2400884. doi:10.1002/lpor.202400884

4. Park J, Lee KR, Park YK. Ultrathin wide-angle large-area digital 3D holographic display using a non-periodic photon sieve. *Nat Commun* (2019) 10(1):1304. doi:10.1038/s41467-019-09126-9

5. Zhang C, Zhang D, Bian Z. Dynamic full-color digital holographic 3D display on single DMD. *Opto-electron Adv* (2021) 4(3):200049–7. doi:10.29026/oea.2021.200049

6. Tay S, Blanche PA, Voorakaranam R, Tunç AV, Lin W, Rokutanda S, et al. An updatable holographic three-dimensional display. *Nature* (2008) 451(7179):694–8. doi:10.1038/nature06596

7. Cornish WD. *The photorefractive effect in lithium niobate [dissertation]*. Vancouver: University of British Columbia (1976).

8. Tsutsumi N. Recent advances in photorefractive and photoactive polymers for holographic applications. *Polym Int* (2017) 66(2):167–74. doi:10.1002/pi.5096

9. Blanche PA, Bablumian A, Voorakaranam R, Christenson C, Lin W, Gu T, et al. Holographic three-dimensional telepresence using large-area photorefractive polymer. *Nature* (2010) 468(7320):80–3. doi:10.1038/nature09521

10. Li X, Li Y, Xiang Y, Rong N, Zhou P, Liu S, et al. Highly photorefractive hybrid liquid crystal device for a video-rate holographic display. *Opt Express* (2016) 24(8):8824–31. doi:10.1364/oe.24.008824

11. Kozanecka-Szmigiel A, Rutkowska KA, Nieborek M, Kwasny M, Karpierz MA, Schab-Balcerzak E, et al. Photopatterned azo poly (amide imide) layers as aligning substrates of holographic liquid crystal diffraction gratings for beam steering applications. *J Mater Chem C* (2020) 8(3):968–76. doi:10.1039/c9tc04296b

12. Kong Y, Bo F, Wang W, Zheng D, Liu H, Zhang G, et al. Recent progress in lithium niobate: optical damage, defect simulation, and on-chip devices. *Adv Mater* (2020) 32(3):1806452. doi:10.1002/adma.201806452

13. Kong Y, Liu S, Xu J. Recent advances in the photorefraction of doped lithium niobate crystals. *Materials* (2012) 5(10):1954–71. doi:10.3390/ma5101954

14. Boes A, Chang L, Langrock C, Yu M, Zhang M, Lin Q, et al. Lithium niobate photonics: unlocking the electromagnetic spectrum. *Science* (2023) 379(6627):eabj4396. doi:10.1126/science.abj4396

15. Weigand H, Vogler-Neuling VV, Escalé MR, Pohl D, Richter FU, Karvounis A, et al. Enhanced electro-optic modulation in resonant metasurfaces of lithium niobate. *ACS Photon* (2021) 8(10):3004–9. doi:10.1021/acsphotonics.1c00935

16. Feng H, Zhang K, Sun W, Ren Y, Zhang Y, Zhang W, et al. Ultra-high-linearity integrated lithium niobate electro-optic modulators. *Photon Res* (2022) 10(10):2366–73. doi:10.1364/prj.464650

17. Qu L, Wu W, Cai W, Ren M, Xu J. Second harmonic generation in lithium niobate on insulator. *Laser and Photon Rev* (2025) 19:2401928. doi:10.1002/lpor.202401928

18. Zhang X, Mugisha ER, Mi Y, Liu X, Wang M, Gao Z, et al. Photovoltaic cycling to-and-fro actuation of a water-microdroplet for automatic repeatable solute acquisition on oil-infused hydrophobic LN: fe surface. *ACS Photon* (2021) 8(2):639–47. doi:10.1021/acsphotonics.0c01781

19. Wang C, Zhang M, Chen X, Bertrand M, Shams-Ansari A, Chandrasekhar S, et al. Integrated lithium niobate electro-optic modulators operating at CMOS-Compatible voltages. *Nature* (2018) 562(7725):101–4. doi:10.1038/s41586-018-0551-y

20. Tan Y, Niu S, Billet M, Singh N, Niels M, Vanackere T, et al. Micro-transfer printed thin film lithium niobate (TFLN)-on-silicon ring modulator. *ACS Photon* (2024) 11(5):1920–7. doi:10.1021/acsphotonics.3c01869

21. He M, Xu M, Ren Y, Jian J, Ruan Z, Xu Y, et al. High-performance hybrid silicon and lithium niobate mach–zehnder modulators for 100 gbit s^{-1} and beyond. *Nat Photon.* (2019) 13(5):359–64. doi:10.1038/s41566-019-0378-6

22. Hou S, Hu H, Liu Z, Xing W, Zhang J, Hao Y. High-speed electro-optic modulators based on thin-film lithium niobate. *Nanomaterials* (2024) 14(10):867. doi:10.3390/nano14100867

23. Smalley DE, Smithwick QYJ, Bove VM, Barabas J, Jolly S. Anisotropic leaky-mode modulator for holographic video displays. *Nature* (2013) 498(7454):313–7. doi:10.1038/nature12217

24. Gao R, Zhang H, Bo F, Fang W, Hao Z, Yao N, et al. Broadband highly efficient nonlinear optical processes in on-chip integrated lithium niobate microdisk resonators of Q-factor above 10^8. *New J Phys* (2021) 23(12):123027. doi:10.1088/1367-2630/ac3d52

25. Xu Y, Shen M, Lu J, Surya JB, Sayem AA, Tang HX. Mitigating photorefractive effect in thin-film lithium niobate microring resonators. *Opt Express* (2021) 29(4):5497–504. doi:10.1364/oe.418877

26. Zhang Y, Luo Q, Zheng D, Wang S, Liu S, Liu H, et al. Highly efficient on-chip erbium–ytterbium co-doped lithium niobate waveguide amplifiers. *Photon Res* (2023) 11(10):1733–7. doi:10.1364/prj.497947

27. Luo R, Jiang H, Rogers S, Liang H, He Y, Lin Q. On-chip second-harmonic generation and broadband parametric down-conversion in a lithium niobate microresonator. *Opt Express* (2017) 25(20):24531–9. doi:10.1364/oe.25.024531

28. Xie Z, Bo F, Lin J, Hu H, Cai X, Tian XH, et al. Recent development in integrated lithium niobate photonics. *Adv Phys X* (2024) 9(1):2322739. doi:10.1080/23746149.2024.2322739

29. Kong Y, Wu S, Liu S, Chen S, Xu J. Fast photorefractive response and high sensitivity of Zr and Fe codoped $LiNbO_3$ crystals. *Appl Phys Lett* (2008) 92:251107. doi:10.1063/1.2952275

30. Dong Y, Liu S, Li W, Kong Y, Chen S, Xu J. Improved ultraviolet photorefractive properties of vanadium-doped lithium niobate crystals. *Opt Lett* (2011) 36(10):1779–81. doi:10.1364/ol.36.001779

31. Tian T, Kong Y, Liu S, Li W, Wu L, Chen S, et al. Photorefraction of molybdenum-doped lithium niobate crystals. *Opt Lett* (2012) 37(13):2679–81. doi:10.1364/ol.37.002679

32. Zheng D, Kong Y, Liu S, Chen M, Chen S, Zhang L, et al. The simultaneous enhancement of photorefraction and optical damage resistance in MgO and Bi_2O_3 co-doped $LiNbO_3$ crystals. *Sci Rep* (2016) 6:20308. doi:10.1038/srep20308

33. Wang S, Shan Y, Wang W, Zheng D, Liu H, Liu S, et al. Lone-pair electron effect induced a rapid photorefractive response in site-controlled $LiNbO_3$:Bi,M (M = Zn, In, zr) crystals. *Appl Phys Lett* (2021) 118:191902. doi:10.1063/5.0048638

34. Wang S, Shan Y, Wu Z, Zheng D, Liu S, Liu H, et al. Enhanced red-light photorefractive response speed of LiNbO3 crystals for full color holographic display. *Appl Phys Lett* (2025) 126:011904. doi:10.1063/5.0233431

35. Zheng D, Wang W, Wang S, Liu H, Kong Y. Real-time dynamic holographic display realized by bismuth and magnesium co-doped lithium niobate. *Appl Phys Lett* (2019) 114:241903. doi:10.1063/1.5107460

36. Wang S, Shan Y, Zheng D, Liu S, Bo F, Liu H, et al. The real-time dynamic holographic display of LN:Bi,Mg crystals and defect-related electron mobility. *Opto-electron Adv* (2022) 5:210135. doi:10.29026/oea.2022.210135

37. Kresse G, Furthmu¨ller J. Efficiency of *ab-initio* total energy calculations for metals and semiconductors using a plane-wave basis set. *Comput Mater Sci* (1996) 6:15–50. doi:10.1016/0927-0256(96)00008-0

38. Kresse G, Furthmu¨ller J. Efficient iterative schemes for *ab initio* total-energy calculations using a plane-wave basis set. *Phys Rev B* (1996) 54:11169–86. doi:10.1103/physrevb.54.11169

39. Kresse G, Joubert D. From ultrasoft pseudopotentials to the projector augmented-wave method. *Phys Rev B* (1999) 59:1758–75. doi:10.1103/physrevb.59.1758

40. Perdew JP, Burke K, Ernzerhof M. Generalized gradient approximation made simple. *Phys Rev Lett* (1996) 77:3865–8. doi:10.1103/physrevlett.77.3865

41. Földvári I, Polgár K, Voszka R, Balasanyan RN. A simple method to determine the real composition of $LiNbO_3$ crystals. *Cryst Res Technol* (1984) 19:1659–61. doi:10.1002/crat.2170191231

42. Polgár K, Kovács L, Földvári I, Cravero I. Spectroscopic and electrical conductivity investigation of Mg doped $LiNbO_3$ single crystals. *Solid State Commun* (1986) 59:375–9. doi:10.1016/0038-1098(86)90566-1

43. Li X, Kong Y, Liu H, Sun L, Xu J, Chen S, et al. Origin of the generally defined absorption edge of non-stoichiometric lithium niobate crystals. *Solid State Commun* (2007) 141(3):113–6. doi:10.1016/j.ssc.2006.10.021

44. Chen K, Li Y, Peng C, Lu Z, Luo X, Xue D. Microstructure and defect characteristics of lithium niobate with different li concentrations. *Inorg Chem Front* (2021) 8(17):4006–13. doi:10.1039/d1qi00562f

45. Kim JS, Ho PKH, Thomas DS, Friend R, Cacialli F, Bao GW, et al. X-ray photoelectron spectroscopy of surface-treated indium-tin oxide thin films. *Chem Phys Lett* (1999) 315(5-6):307–12. doi:10.1016/s0009-2614(99)01233-6

46. Yan S, Ge S, Zuo Y, Qiao W, Zhang L. Effects of carbothermal annealing on structure defects, electrical and magnetic properties in Fe-doped In_2O_3. *Scripta Mater* (2009) 61(4):387–90. doi:10.1016/j.scriptamat.2009.04.022

47. Bu D, Fu Y, Sun N, Li Y, An Y, Liu J. Effect of Cu doping on room temperature ferromagnetic behavior of Mn doped $LiNbO_3$ films. *J Cryst Growth* (2016) 453:198–202. doi:10.1016/j.jcrysgro.2016.06.054

48. Fan Y, Li L, Li Y, Sun X, Zhao X. Hybrid density functional theory study of vanadium doping in stoichiometric and congruent $LiNbO_3$. *Phys Rev B* (2019) 99:035147. doi:10.1103/physrevb.99.035147

49. Van de Walle CG, Neugebauer J. First-principles calculations for defects and impurities: applications to III-Nitrides. *J Appl Phys* (2004) 95:3851–79. doi:10.1063/1.1682673